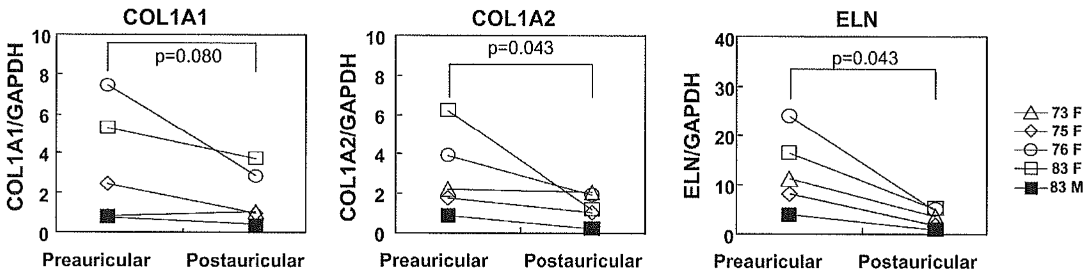

Fig. 2 Gene expression of procollagen and tropoelastin in the postauricular and preauricular skin. Total RNA were extracted from the postauricular and preauricular skin of the same subjects (n = 5), and applied to quantitative real-time PCR. Symbols shows age and sex of each subject. COL1A1, Type I collagen α1 subunit; COL1A2, Type I collagen α2 subunit; ELN, tropoelastin; GAPDG, glyceraldehydes-3-phosphate dehydrogenase

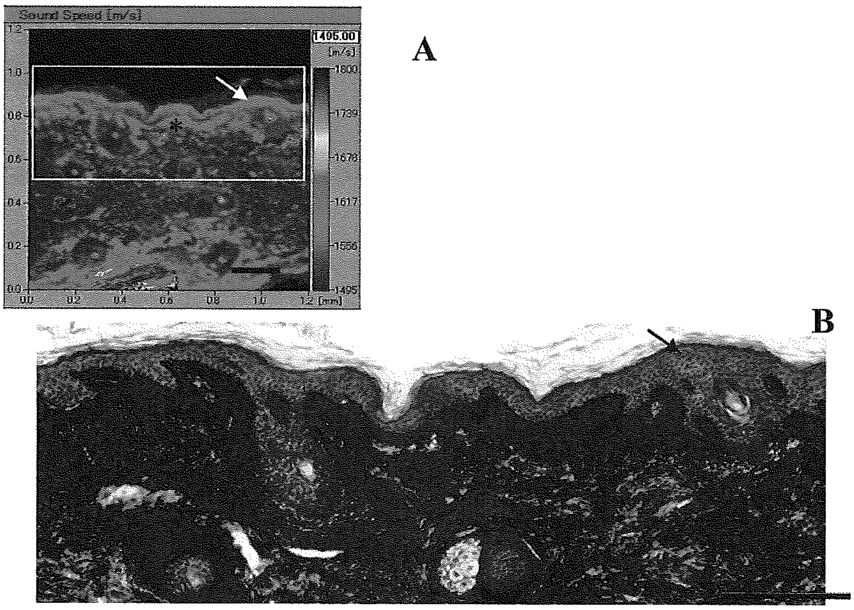

Fig. 3 Two-dimensional distribution of ultrasonic velocity and EVG staining of postauricular skin (66 year-old female). **A**, ultrasonic velocity; **B**, EVG stain. Higher ultrasonic velocity was observed in the uppermost of the stratum granulosum (arrow) and collagen layer beneath the epidermis (*).

RESULTS

To confirm the status of photodamage of aged preauricular skin, elastin and procollagen mRNA were measured by real-time PCR. The mRNA level of elastin in the preauricular skin was markedly increased compared with the postauricular skin (Fig. 2). Contrary to our expectations, the mRNA level of collagen α2 (I) in the preauricular skin was significantly increased and the mRNA level of collagen α1 (I) in the preauricular skin also tend to be increased, compared with the postauricular skin.

Figure 3 shows EVG staining and the acoustic image of postauricular skin (photoprotected area) of a female (66 years old). The sound speed varied from about 1500 to 1600 m/s in the tissue. The uppermost layer of keratinocytes and the dermis beneath the epidermis showed a relatively higher sound speed (light blue). The uppermost layer of keratinocytes seemed to coincide with the granular layer in the epidermis. The collagen

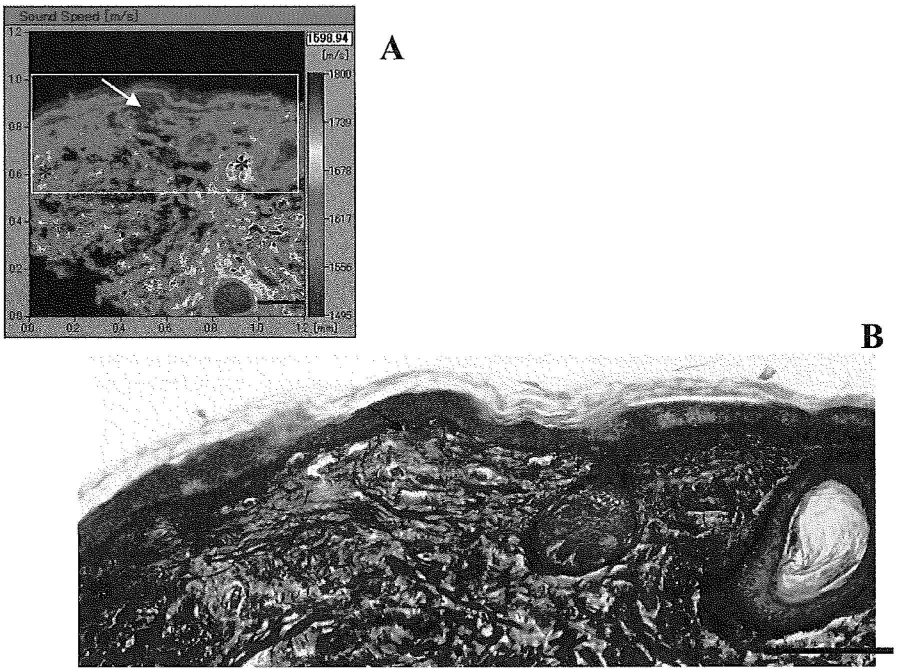

Fig. 4 Two-dimensional distribution of ultrasonic velocity and EVG staining of buttock skin. **A**, ultrasonic velocity; **B**, EVG stain. Decreased ultrasonic velocity was observed in the thin collagen layer beneath the epidermis (arrow). Higher ultrasonic velocity was observed in the dunning thick collagen fibers in the deeper dermis (*). Scale, 200μm

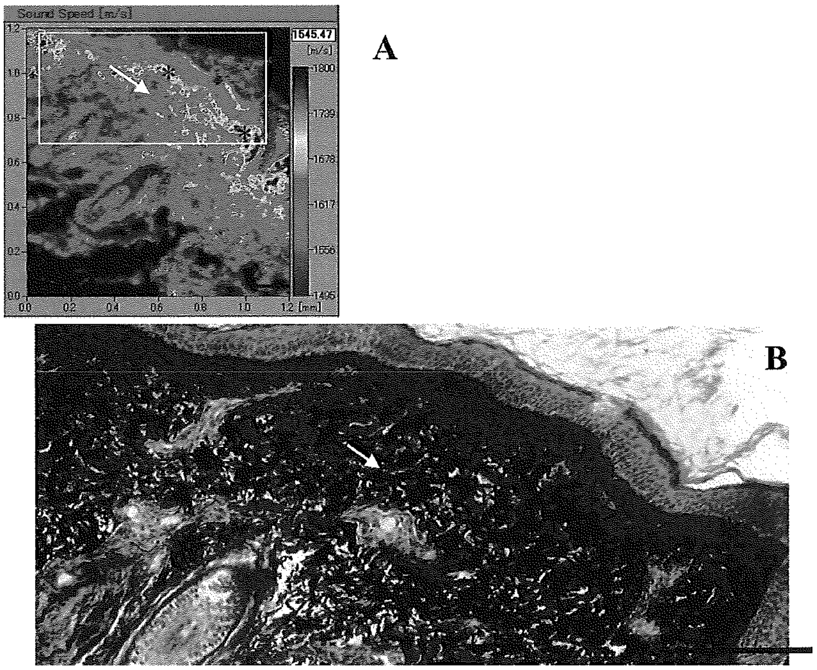

Fig. 5 Two-dimensional distribution of ultrasonic velocity and EVG staining of preauricular skin of subject shown in Fig. 3. **A**, ultrasonic velocity; **B**, EVG stain. Increased ultrasonic velocity in the Grenz zone (*) and decreased ultrasonic velocity in the solar elastosis were observed (arrow). Scale, 200μm

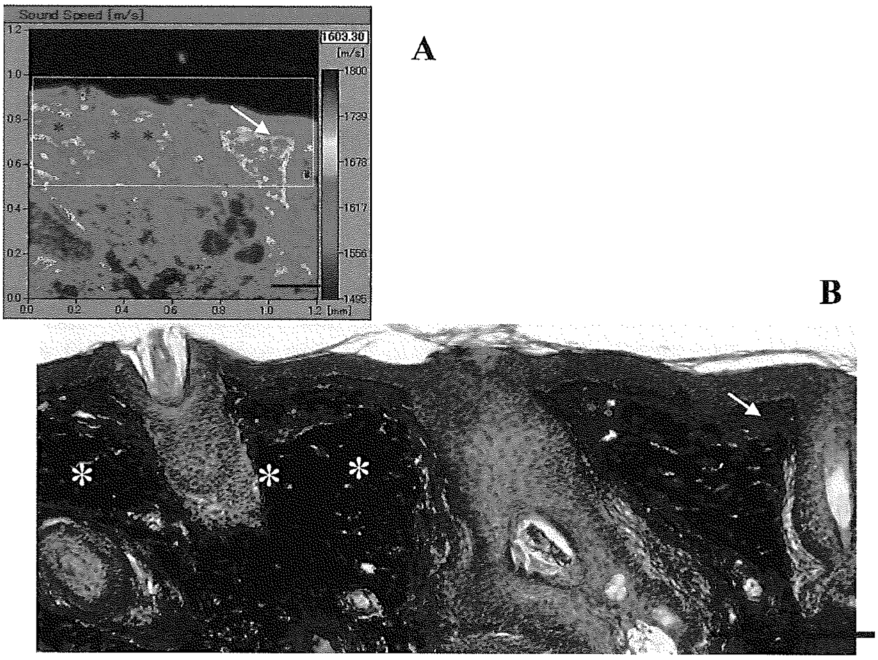

Fig. 6 Two-dimensional distribution of ultrasonic velocity and EVG staining of preauricular skin (69 year-old male). **A**, ultrasonic velocity; **B**, EVG stain. Increased ultrasonic velocity in the Grenz zone (arrow) and decreased ultrasonic velocity in part of the solar elastosis were observed (*). Scale, 200μm

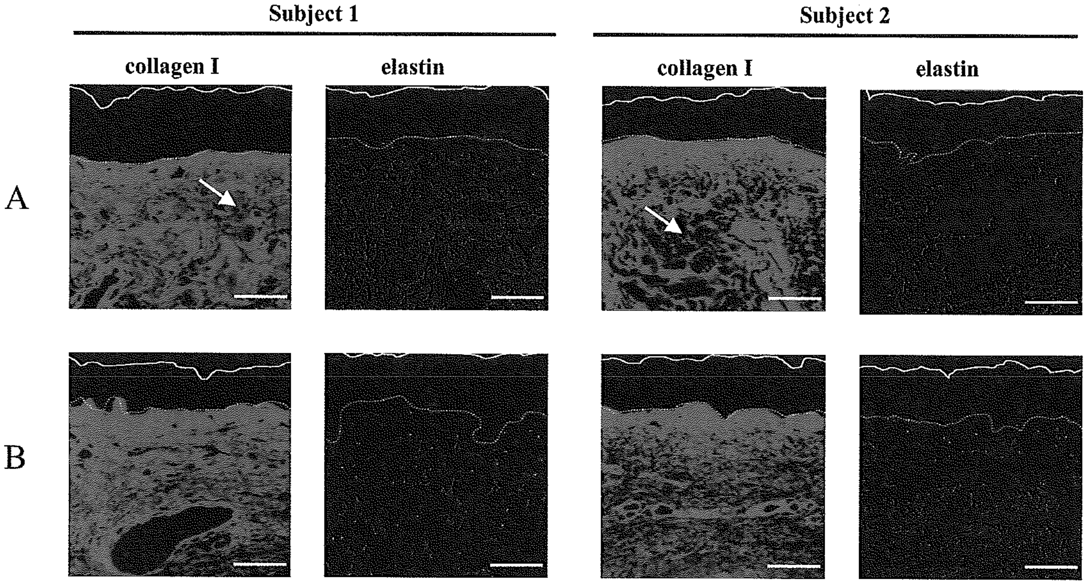

Fig. 7 Protein expression of procollagen and tropoelastin in postauricular and auricular skin. Preauricular (**A**) and postauricular skin (**B**) was obtained from subject 1 (shown in Fig. 3 and 5) and subject 2 (shown in Fig. 6). Procollagen (green) and tropoelastin (red) were stained immunohistochemically using corresponding antibodies. The dashed line shows the dermo-epidermal junction. The solid line shows the surface of the skin. Decreased signal (arrow) was observed at the site of solar elastosis. Scale, 100μm.

layer in the dermis beneath the epidermis had hardly any anchoring structure of oxytalan fibers as seen in the buttock skin (Fig. 3) but maintained an sound speed of about 1600 m/s, suggesting that the collagen layer sustained the physical strength of tissue. Figure 4 shows images of buttock skin (photo-protected area) of a female (69 years old). A decrease in sound speed was observed in the thin collagen layer without a progressive anchoring structure of oxytalan fibers. In the deeper dermis, higher sound speed (more than 1700 m/s) was observed in the thicker collagen fiber.

Figure 5 shows images of preauricular skin (photodamaged area) of a female (66 years old). The Grenz zone, which is a hallmark of photodamage, was developed on a clump of degenerated thick elastic fibers. The Grenz zone showed a higher sound speed (more than 1700 m/s). A decrease in the sound speed in part of the solar elastosis was observed. In the other case of preauricular skin (Fig. 6, 69 year-old male), solar elastosis was highly developed and the Grenz zone could be distinguished clearly by the sound speed (yellow to red).

To investigate the collagen content in the Grenz zone, skin samples were immunohistochemically stained using the antibody for collagen I. This antibody showed a stronger signal in the papillary dermis than in the deeper dermis both in the preauricular and postauricular skin (Fig. 7). The Grenz zone was clearly distinguished from the site of the deposition of elastin as seen by EVG staining in the preauricular skin. The Grenz zone conserved the signal of collagen I even in the more photodamaged preauricular skin (Fig. 7, subject 2). Deeper dermis showed a decreased signal of collagen I in part of the solar elastosis site.

DISCUSSION

In the present study, we first demonstrated the two-dimensional sound speed images of skin tissue at the microscopic level using scanning acoustic microscopy. We found four characteristic properties of sound speed in the skin as follows; (1) high sound speed of the keratinizing layer in the uppermost layer of the stratum granulosum, (2) discontinuous distribution of sound speed in the collagen layer beneath the epidermis in aged skin, (3) high sound speed associated with thick collagen fibers in the deeper dermis, and (4) an increase in the sound speed in the Grenz zone in photodamaged skin.

On the assumption that biological tissue is fluid-like, the sound speed is considered to be:

$$C = \sqrt{(K/\rho)} \qquad (7).$$

where C is the sound speed, K is the elastic bulk modulus and ρ is the density. High molecular mass and highly elastic components in the skin increase the sound speed. Saijo *et al.* reported high sound speed associated with stiffness in fibrotic sites in the tissue of the infarcted myocardium. The sound speed is considered depend on the content and quality of collagen fibers [11]. In fact the intensity (dark pink color) of the EVG stain is almost coincident to with the sound speed in this study. Increased sound speed was associated with thicker collagen fiber in the deeper dermis of buttock skin.

The sound speed of the keratinizing layer on the uppermost layer of the stratum granulosum may reflect the condition of differentiation of keratinocytes because keratinocytes produce and cross-link with keratin and components of the cornified envelope in the terminal differentiation to corneocytes to produce rigid stratum corneum [13]. Cross-linking of the cornified envelope may be a polymerizing process influencing the sound speed. A discontinuous layer of sound speed is sometimes observed in the skin, suggesting the heterogeneous keratinizing state of the stratum corneum on the surface of the skin.

We choose postauricular skin as photo-protected skin. We confirmed markedly extremely increased expression of elastin gene in the preauricular skin, compared with the postauricular skin. Generally, buttock or forearm skin is often used as photo-protected skin in the study of photoaging. but there are few reports demonstrating a comparison between postauricular skin and preauricular skin. Bhawan *et al.* pointed structural differences between facial skin and forearm skin as photodamaged skin [1, 12]. When compared with buttock skin, postauricular skin has some differences as follows; (1) less anchoring structure of oxytalan fibers beneath the epidermis, (2) low content of elastic fibers and (3) a decrease in the sound speed in the dermis, suggesting that there is a difference not only in the structure but also in physical properties. Disappearance of the anchoring structure of oxytalan fibers beneath the epidermis and decreased content of elastic fibers are the main changes in intrinsically aged skin [14]. The postauricular skin is reasonable as photo-protected skin compared with buttock skin.

Interestingly, in the postauricular skin, the papillary dermis showed a higher sound speed than that of deeper dermis. This zone is considered to be a site where newly synthesized collagen is localized [15, 16]. We also confirmed an intensive immunochemical signal of collagen I in the papillary dermis in the postauricular skin. This zone may have an important role in sustaining the strength of the skin. Alternately, the decrease in the sound speed was observed in the thin collagen layer without an anchoring structure of oxytalan fibers in the buttock skin, suggesting that the progression of oxytalan fiber may be related to the synthesis of collagen and the strength of collagen fibers.

Photodamaged skin shows hallmarks such Grenz zone formation and solar elastosis [17], but the physiological function of this zone has been not clarified. We first found that the Grenz zone showed a higher sound speed more than the site of solar elastosis, and that the sound speed in part of the solar elastosis was actually decreased. Moreover, we detected deposition of collagen I in the Grenz zone even in the more photodamaged preauricular skin. These results suggest that the fibrosis in the Grenz zone compensates the strength of tissue with the progress of solar elastosis. Photoaging brings a decreased elasticity of the skin. Ultraviolet rays are considered to promote the decrease in the collagen content [2], degeneration of collagen fibers [3], and accumulation of degenerated elastin [18]. In the Grenz zone, type I collagen synthesis is considered to be depressed in photodamaged skin [2, 16] and degenerated collagen fibers are observed [19, 20]. Type VII collagen synthesis is also reported to be depressed [21], although some reports demonstrate that the synthesis of type I collagen [22], type III collagen [23] and type VI collagen [24] is maintained in the Grenz zone. These discrepancies may be due to the status of photodamage and/or the examined site. We detected overall increased expression of collagen gene and conserved deposition of collagen I in the Grenz zone in the preauricular skin. Chung *et al.* also reported an increase in the collagen mRNA level in photoaged skin [22]. They argued that the degradation of collagen by MMPs was activated in the photodamaged skin. But localized modification of collagen may also take place in photodamaged skin. At least, the Grenz zone seems to exhibit different collagen metabolism than the the deeper dermis in photodamaged skin. Lavker emphasized that the Grenz zone, which had packed collagen fibrils in colinear arrangement, was a fibrosis-like microscar [17]. The Grenz zone may not be simply damaged, and rather plays an important role in sustaining the physical strength of photodamaged skin by rescuer fibrosis.

In conclusion, this study is the first to demonstrate the change of heterogeneous physical strength in the photodamaged skin using the SAM system. The SAM system will did in clarification of the role of structural proteins in photodamaged skin.

REFERENCES

1) Bhawan J, Andersen W, Lee J, Labadie R, Solares G. Photoaging versus intrinsic aging: a morphologic assessment of facial skin. J Cutan Pathol 1995; 22(2): 154-9.
2) Talwar HS, Griffiths CE, Fisher GJ, Hamilton TA, Voorhees JJ. Reduced type I and type III procollagens in photodamaged adult human skin. J Invest Dermatol 1995; 105(2): 285-90.
3) Nishimori Y, Edwards C, Pearse A, Matsumoto K, Kawai M, Marks R. Degenerative alterations of dermal collagen fiber bundles in photodamaged human skin and UV-irradiated hairless mouse skin: possible effect on decreasing skin mechanical properties and appearance of wrinkles. J Invest Dermatol 2001; 117(6): 1458-63.
4) Imokawa G, Takema Y, Yorimoto Y, Tsukahara K, Kawai M, Imayama S. Degree of ultraviolet-induced tortuosity of elastic fibers in rat skin is age dependent. J Invest Dermatol 1995; 105(2): 254-8.
5) Inomata S, Matsunaga Y, Amano S, Takada K, Kobayashi K, Tsunenaga M, *et al.* Possible involvement of gelatinases in basement membrane damage and wrinkle formation in chronically ultraviolet B-exposed hairless mouse. J Invest Dermatol 2003; 120(1): 128-34.
6) Cua AB, Wilhelm KP, Maibach HI. Elastic properties of human skin: relation to age, sex, and anatomical region. Arch Dermatol Res 1990; 282(5): 283-8.
7) Holbrook KA, Byers PH. Skin is a window on heritable disorders of connective tissue. Am J Med Genet 1989; 34(1): 105-21.
8) Ushiki T. Collagen fibers, reticular fibers and elastic fibers. A comprehensive understanding from a

morphological viewpoint. Arch Histol Cytol 2002; 65(2): 109-26.

9) Verdonk ED, Wickline SA, Miller JG. Anisotropy of ultrasonic velocity and elastic properties in normal human myocardium. J Acoust Soc Am 1992; 92(6): 3039-50.

10) Hoffmeister BK, Verdonk ED, Wickline SA, Miller JG. Effect of collagen on the anisotropy of quasi-longitudinal mode ultrasonic velocity in fibrous soft tissues: a comparison of fixed tendon and fixed myocardium. J Acoust Soc Am 1994; 96(4): 1957-64.

11) Saijo Y, Sasaki H, Naganuma T, Tanaka M. Ultrasonic tissue characterization of diseased myocardium by scanning acoustic microscopy. J Cardiol 1995; 25(3): 127-32.

12) Bhawan J, Oh CH, Lew R, Nehal KS, Labadie RR, Tsay A, *et al.* Histopathologic differences in the photoaging process in facial versus arm skin. Am J Dermatopathol 1992; 14(3): 224-30.

13) Nemes Z, Steinert PM. Bricks and mortar of the epidermal barrier. Exp Mol Med 1999; 31(1): 5-19.

14) Kligman AM, Zheng P, Lavker RM. The anatomy and pathogenesis of wrinkles. Br J Dermatol 1985; 113(1): 37-42.

15) Kligman LH. Effects of all-trans-retinoic acid on the dermis of hairless mice. J Am Acad Dermatol 1986; 15(4 Pt 2): 779-85, 884-7.

16) Nelson BR, Majmudar G, Griffiths CE, Gillard MO, Dixon AE, Tavakkol A, *et al.* Clinical improvement following dermabrasion of photoaged skin correlates with synthesis of collagen I. Arch Dermatol 1994; 130(9): 1136-42.

17) Lavker RM. Structural alterations in exposed and unexposed aged skin. J Invest Dermatol 1979; 73(1): 59-66.

18) Bernstein EF, Chen YQ, Tamai K, Shepley KJ, Resnik KS, Zhang H, *et al.* Enhanced elastin and fibrillin gene expression in chronically photodamaged skin. J Invest Dermatol 1994; 103(2): 182-6.

19) Bernstein EF, Chen YQ, Kopp JB, Fisher L, Brown DB, Hahn PJ, *et al.* Long-term sun exposure alters the collagen of the papillary dermis. Comparison of sun-protected and photoaged skin by northern analysis, immunohistochemical staining, and confocal laser scanning microscopy. J Am Acad Dermatol 1996; 34(2 Pt 1): 209-18.

20) Yamamoto O, Bhawan J, Solares G, Tsay AW, Gilchrest BA. Ultrastructural effects of topical tretinoin on dermo-epidermal junction and papillary dermis in photodamaged skin. A controlled study. Exp Dermatol 1995; 4(3): 146-54.

21) Craven NM, Watson RE, Jones CJ, Shuttleworth CA, Kielty CM, Griffiths CE. Clinical features of photodamaged human skin are associated with a reduction in collagen VII. Br J Dermatol 1997; 137(3): 344-50.

22) Chung JH, Seo JY, Choi HR, Lee MK, Youn CS, Rhie G, *et al.* Modulation of skin collagen metabolism in aged and photoaged human skin in vivo. J Invest Dermatol 2001; 117(5): 1218-24.

23) El-Domyati M, Attia S, Saleh F, Brown D, Birk DE, Gasparro F, *et al.* Intrinsic aging vs. photoaging: a comparative histopathological, immunohistochemical, and ultrastructural study of skin. Exp Dermatol 2002; 11(5): 398-405.

24) Watson RE, Ball SG, Craven NM, Boorsma J, East CL, Shuttleworth CA, *et al.* Distribution and expression of type VI collagen in photoaged skin. Br J Dermatol 2001; 144(4): 751-9.

ACOUSTIC MICROSCOPY BASED ON FREQUENCY DOMAIN ANALYSIS OF A SINGLE PULSED WAVE

Y. Saijo*, N. Hozumi**, K. Kobayashi***, N. Okada***, K. Fukuma****,
N. Tanaka*****, H. Sasaki*, M. Tanaka*, and T. Yambe*

* Department of Medical Engineering and Cardiology, Institute of Development, Aging and Cancer,
Tohoku University, Sendai, Japan
** Toyohashi University of Technology, Toyohashi, Japan
*** Honda Electronics Co. Ltd., Toyohashi, Japan
**** TrafficSim Co. Ltd., Nagoya, Japan
***** Shibaura Institute of Technology, Omiya, Japan

E-Mail Address: saijo@idac.tohoku.ac.jp

Abstract: Scanning acoustic microscopy (SAM) for biomedicine is useful for intra-operative pathological examination, understanding of lower frequency ultrasonic images, and assessment of biomechanics at a microscopic level. Recently, we have proposed a new concept SAM utilizing a single pulsed wave instead of continuous waves used in conventional SAM systems. Speed of sound images of 300x300 pixels were successfully obtained within 150 sec.

Introduction

Since 1985, we have been developing a scanning acoustic microscope (SAM) system for biomedical use and have been investigating acoustic properties of various organs and various disease states with this SAM system [1-2]. SAM for biomedicine is useful for intra-operative pathological examination, understanding of lower frequency ultrasonic images, and assessment of biomechanics at a microscopic level. The originality of our traditional SAM system is that it can provide quantitative values of attenuation and sound speed of a thinly sliced soft tissue.

Recently, we have proposed a new concept SAM utilizing a single pulsed wave instead of continuous waves used in conventional SAM systems [3]. Here, we present example images of some kinds of pathological specimens.

Materials and Methods

System: Figure 1 shows a block diagram of sound speed microscopy for biological tissue characterization. A single pulsed ultrasound with 5 ns pulse width was emitted and received by the same transducer above the specimen. The aperture diameter of the transducer was 1.2 mm and the focal length was 1.5 mm. The central frequency was 80 MHz and the pulse repetition rate was 10 kHz. Considering focal distance and the sectional area of the transducer, the diameter of focal spot was estimated as 20 micron at 80 MHz. Distilled water was used as the coupling medium between the transducer and the specimen. The reflections from the tissue surface and from the interface between tissue and glass were received by the transducer and were introduced into a digital oscilloscope (Tektronics TDS 5052, USA). The frequency range was 300 MHz and the sampling rate was 2.5 GS/s. Four times of pulse responses at the same point were averaged in the oscilloscope in order to reduce random noise.

The transducer was mounted on an X-Y stage with a microcomputer board which was driven by the computer installed in the digital oscilloscope through RS-232C. X-scan was driven by a linear servo-motor and Y-scan was driven by a stepping motor. Finally, two-dimensional distributions of ultrasonic intensity, sound speed and thickness of the specimen of 2.4 by 2.4 mm area were visualized with 300 by 300 pixels. Total scanning time was 150 sec.

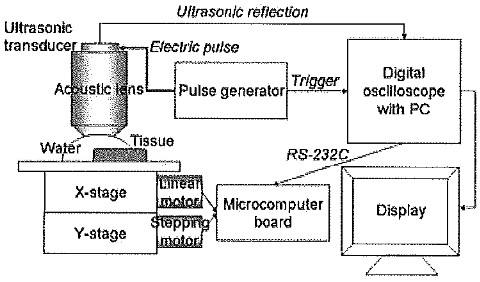

Figure 1: Block diagram of the system

Signal Analysis: The reflected wave at the glass surface without tissue was employed as a reference waveform. The wave from the tissue area contained two reflections at the surface and the interface of tissue and glass. The frequency domain analysis was performed by analyzing interference between two components which cannot be separated in time domain analysis. Intensity and phase spectra were calculated by Fourier-transforming the waveform. The spectra were normalized by the reference waveform. Figure 2 shows the frequency domain analysis of interfered waves.

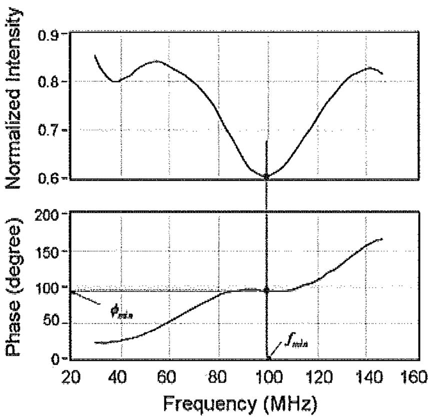

Figure 2: Frequency domain analysis of interfered waves

Assuming f_{min} as the minimum point in the intensity spectrum, and ϕ_{min} as the corresponding phase angle, the phase difference between the two reflections at the minimum point is $(2n\text{-}1)\pi$, giving

$$2\pi f_{min} \times \frac{2d}{c_0} = \phi_{min} + (2n-1)\pi \cdots (1)$$

where d, c_0, and n are the tissue thickness, sound speed of the water, and a non-negative integer, respectively. The phase angle ϕ_{min} can be expressed by

$$2\pi f_{min} \times 2d\left(\frac{1}{c_0} - \frac{1}{c}\right) = \phi_{min} \cdots (2)$$

since ϕ_{min} is the phase difference between the wave passed through the distance $2d$ with sound speed c and that passed through the corresponding distance with sound speed c_0. By solving the equations (1) and (2),

$$d = \frac{c_0}{4\pi f_{min}}\{\phi_{min} + (2n-1)\pi\} \cdots (3)$$

is obtained. Speed of sound at the minimum point frequency is finally calculated as

$$c = \left(\frac{1}{c_0} - \frac{\phi_{min}}{4\pi f_{min} d}\right) \cdots (4)$$

Results

Figure 3 is a snapshot of the PC window showing a SAM image. The upper left is the intensity image, the upper middle is the speed of sound image, the upper right is the waveform, and the lower middle is the thickness image, respectively. The example is breast cancer with scirrhous change. The speed of sound is 1700 m/s at the fibrotic lesion while that is 1560 m/s in the ductus area.

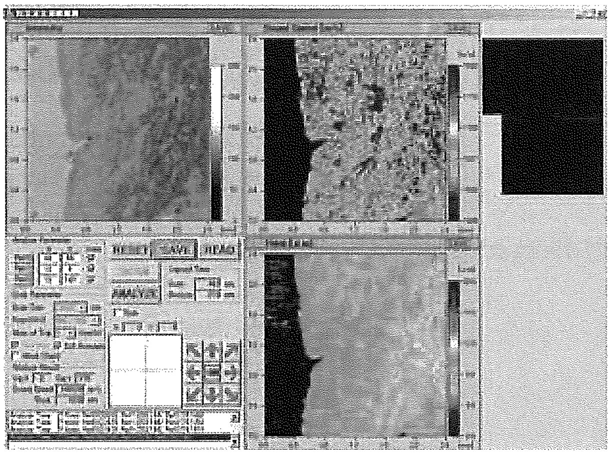

Figure 3: A snapshot of the PC window showing a SAM image

Discussion

The speed of sound image obtained with the new concept SAM showed physical characteristics of breast cancer with scirrhous change. Fibrotic lesion showed higher speed of sound than normal breast ductus area. The data acquisition of one frame was 8sec in conventional SAM and 150 sec in speed of sound SAM. However, the operator of conventional SAM required a skill, for example, to correct tilting of specimen. The correction of tilting was done automatically in sound speed microscopy and the user interface was friendly to medical and pathological researcher.

Conclusions

An acoustic microscope system which can measure sound speed of thinly sliced biological material was developed. It was a unique acoustic microscope because it used a single pulse and Fourier transform to calculate sound speed at all the measuring points. Although the data acquisition time of one frame was longer than the conventional SAM, total time for calculation was significantly shorter. It can be applied to intra-operative pathological examination.

References

[1] SAIJO Y, TANAKA M, OKAWAI H, SASAKI H, NITTA S, DUNN F (1997) 'Ultrasonic tissue characterization of infarcted myocardium by scanning acoustic microscopy', *Ultrasound Med Biol* **23** pp. 77-85.

[2] SAIJO Y, MIYAKAWA T, SASAKI H, TANAKA M, NITTA S (2004) 'Acoustic properties of aortic aneurysm obtained with scanning acoustic microscopy', *Ultrasonics* **42** pp. 695-698.

[3] HOZUMI N, YAMASHITA R, LEE CK, NAGAO M, KOBAYASHI K, SAIJO Y, TANAKA M, TANAKA N, OHTSUKI S (2004) 'Time-frequency analysis for pulse driven ultrasonic microscopy for biological tissue characterization', *Ultrasonics* **42** pp. 717-722.

FULLY-AUTOMATIC MEASUREMENT OF FLOW MEDIATED DILATATION

Y. Saijo*, Y. Akino**, S. Watanabe**, K. Oba***,
K. Tamamura***, Y. Yamazaki***, and T. Ishiguro****

* Department of Medical Engineering and Cardiology, Institute of Development, Aging and Cancer,
Tohoku University, Sendai, Japan
** Miyagi Social Insurance Hospital, Sendai, Japan
*** Fukuda Denshi Co. Ltd., Tokyo, Japan
**** Chunichi Denshi Co. Ltd., Nagoya, Japan

E-Mail Address: saijo@idac.tohoku.ac.jp

Abstract: Flow mediated dilatation (FMD) is a clinically available, important parameter of vascular endothelial function. However, the measurement of FMD was difficult because skilful and precise measurement based on B-mode ultrasound was required. We propose a novel measuring system of FMD based on change of vascular compliance by analyzing pulsed wave pressure and volume. FMD was successfully obtained in healthy volunteers but the time course was different from that obtained by conventional ultrasound measurement.

Introduction

Flow mediated dilatation (FMD) is a clinically available parameter of vascular endothelial function. FMD is reactive hyperemia caused by releasing nitric oxide (NO) from vascular endothelium after occluding and releasing brachial artery. FMD is a good predictive factor of atherosclerosis and is very sensitive to drug response [1-3]. Previously, FMD has been measured by B-mode ultrasound [4]. However, the measurement required skilful sonographers and the precision of measurement was limited by the frequency of ultrasound.

In the present study, we propose a novel measuring algorithm of FMD based on beat by beat calculation of vascular compliance by analyzing pulsed wave pressure and volume simultaneously.

Materials and Methods

Subjects: Ten healthy volunteers (18-62 years old, male) were involved. Smoking or eating was prohibited before 30 minutes of measurement. Written informed consent was obtained from each volunteer.

Electrocardiogram (ECG): Electrocardiogram was monitored during measurement by conventional electrodes.

Pulsed Wave Volume: Pulsed wave volume was measured by electrical impedance change of the forearm. Two sheet electrodes were attached 10 cm apart on the forearm and electric impedance was measured.

Pulsed Wave Pressure: Pulsed wave pressure was measured by a ceramic piezoelectric sensor attached upon the radial artery.

B-mode Ultrasound: The diameter of brachial artery was measured by conventional B-mode ultrasound with central frequency of 13-MHz as a reference. The probe was fixed upon the brachial artery by a special probe holder.

Experimental Setup: The volunteer was laid on a bed in dark condition with adequate air-conditioning. Blood pressure (BP) was measured and the brachial artery was occluded by a cuff at the pressure 50 mmHg higher than the systolic BP. All the parameters (electrocardiogram, pulsed wave pressure, pulsed wave volume and ultrasound) were recorded before occlusion as control. The occlusion was maintained for 5 minutes. All the parameters were again recorded beat by beat until 15 minutes after occluding brachial artery. Figure 1 shows the experimental setup.

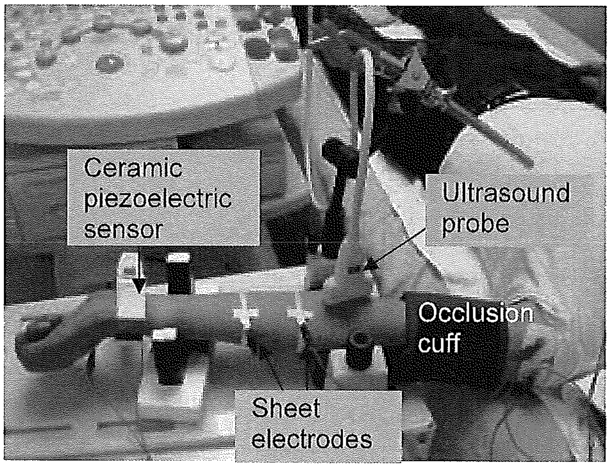

Figure 1: The Experimental Setup

Calculation of FMD: As the vascular compliance can be calculated by equation (1).

$$C = \frac{\Delta V}{\Delta P} = \frac{2\pi R^3(1-\sigma^2)}{Eh} \cdots (1)$$

The radius of the artery can be expressed as equation (2),

$$R = \sqrt[3]{\left(\frac{Eh}{2\pi(1-\sigma^3)}\right)\frac{\Delta V}{\Delta P}} \cdots (2)$$

where ΔV: change of pulsed wave volume, ΔP: change of pulsed wave pressure, R: radius of vessel, h: thckness of vessel wall, E: Young's elastic modulus, σ: Poisson's ratio, respectively. If the changes of R, h, E and σ before and after occlusion were considered very small, the relative change of radius of the vessel is expressed as equation. (3),

$$\% FMD = \frac{R_r - R_c}{R_c} \times 100$$

$$= \frac{\sqrt[3]{\left(\frac{Eh}{2\pi(1-\sigma^3)}\right)\frac{\Delta V_r}{\Delta P_r}} - \sqrt[3]{\left(\frac{Eh}{2\pi(1-\sigma^3)}\right)\frac{\Delta V_c}{\Delta P_c}}}{\sqrt[3]{\left(\frac{Eh}{2\pi(1-\sigma^3)}\right)\frac{\Delta V_c}{\Delta P_c}}} \times 100$$

$$= \left(\sqrt[3]{\frac{P_c \cdot V_r}{P_r \cdot V_c}} - 1\right) \times 100 \cdots (3)$$

where ΔV_c: change of pulsed wave volume at control, ΔP_c: change of pulsed wave pressure at control, R_c: radius of vessel at control, ΔV_r: change of pulsed wave volume after hyperemia, ΔP_r: change of pulsed wave pressure after hyperemia, R_r: radius of vessel after hyperemia, respectively.

Results

None of the subjects was injured nor felt sick in the experiment. Figure 2 shows a result of one of the volunteers (44 years old. male) showing the relation between %FMDus (relative FMD measured by ultrasound) and %FMDimp (relative FMD calculated by the proposed method).

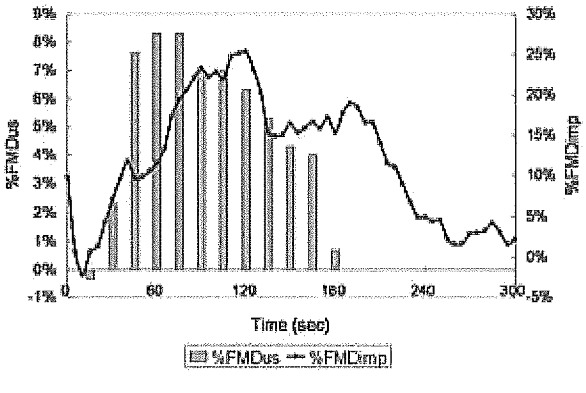

Figure 2: The Result of One of the Volunteers

Biphasic peaks at 120 and 190 sec were observed in %FMDimp while a single peak response was observed at 60 sec after occlusion in %FMDus. The peak was 25% in %FMDimp while it was 8% in %FMDus as reported as normal in the previous studies.

Discussion

Relative FMD (%FMDimp) was successfully obtained by the fully automatic measurement system proposed in the present study. Checking the calculated values beat by beat, the values were robust throughout the measurement. The discrepancy of %FMDimp from %FMDus may be explained that the blood volume of brachial artery alone was not measured by pulsed wave volume. The blood volume of whole vascular system in the forearm including arteries, capillaries, arterioles and veins, may be calculated by pulsed wave volume method. Originally, FMD was caused from the release of NO from occluded region where shear stress was strongly applied. In the sense whole vascular system was affected by NO release, %FMDimp may have its own important meanings in assessment of vascular endothelial function. Also, %FMDimp has a great advantage to conventional FMD measurement because it can be obtained fully automatically.

Conclusions

Relative FMD change (%FMDimp) was automatically measured by analyzing pulsed wave pressure and pulsed wave volume relationship. The result of the calculation was robust and %FMDimp was successfully obtained automatically. Although the peak time and percentage were different from those obtained by conventional ultrasound measurement, %FMDimp may have its own importance in the assessment of vascular endothelial function.

References

[1] FAULX MD, WRIGHT AT, HOIT B. (2003): ‘Detection of endothelial dysfunction with brachial artery ultrasound scanning’, *Am. Heart J.* **145**, pp. 943-51.

[2] BARTH JD. (2001): ‘Which tools are in your cardiac workshop? Carotid ultrasound, endothelial function, and magnetic resonance imaging’, *Am J Cardiol.* **87** pp. 8A-14A.

[3] KIMURA Y, MATSUMOTO M, DEN YB, IWAI K, MUNEHIRA J, HATTORI H, HOSHINO T, YAMADA K, KAWANISHI K, TSUCHIYA H. (1999): ‘Impaired endothelial function in hypertensive elderly patients evaluated by high resolution ultrasonography’, *Can J Cardiol.* **15** pp. 563-8.

[4] JODOIN I, BUSSIERES LM, TARDIF JC, JUNEAU M. (2001): ‘Effect of a short-term primary prevention program on endothelium-dependent vasodilation in adults at risk for atherosclerosis’, *Can J Cardiol.* **15** pp. 83-8.

Acoustic Impedance Micro-imaging for Biological Tissue Using a Focused Acoustic Pulse with a Frequency Range up to 100 MHz

N. Hozumi, A. Kimura, S. Terauchi, M. Nagao, S. Yoshida
Toyohashi University of Technology
Toyohashi, Japan
hozumi@eee.tut.ac.jp

K. Kobayashi
Honda Electronics Co., Ltd.
Toyohashi, Japan

Y. Saijo
Tohoku University
Sendai, Japan

Abstract—**We have proposed a new method for two-dimensional acoustic impedance imaging for biological tissue that can perform micro-scale observation without slicing the specimen. A tissue was placed on a plastic plate of 0.5 mm in thickness. An acoustic pulse with a frequency range up to 100 MHz was transmitted from the "rear side" of the plate, the acoustic beam being focused at the boundary between the tissue and plate. The reflection intensity was interpreted into local acoustic impedance of the target tissue. An acoustic impedance microscopy with 200 x 200 pixels, its field of view being 2 x 2 mm, was obtained by mechanically scanning the transducer. Quantification of acoustic impedance was performed using water or an appropriate material as a reference. The accuracy was evaluated using saline with various NaCl content. A rat cerebellum was employed as the specimen. The development of parallel fiber in cerebella cultures was clearly observed as the contrast in acoustic impedance. The proposed technique is believed to be a powerful tool for biological tissue characterization, as neither staining nor slicing is required.**

Keywords: biological tissue; acoustic impedanc; micro-scale imaging.

I. INTRODUCTION

In most of optical observation of biological tissue, the specimen is sliced into several micrometers in thickness, and fixed on a glass substrate. The microscopy is obtained by transmitted light through the specimen. As it is normally not easy to get a good contrast by local difference in refraction and/or transmission spectrum, the specimen is usually stained before being observed. It can be classified as a kind of chemical imaging, since only a portion that has a specific chemical property can be stained by selecting an appropriate staining material. However, the staining has some disadvantages. It normally takes from several hours to several days to finish the process. Furthermore, the tissue, after being stained, often completely loses its biological functions; i.e., the observation with staining process is chemically destructive.

On the other hand, acoustic imaging can be performed without staining process; i.e., it is chemically non-destructive. The observation can be finished in a very short time, as it does not need the staining process. The idea of ultrasonic microscopy for biological tissue is based on this advantage, and it is considered to become a powerful tool for tissue characterization that can image elastic parameters. Most of ultrasonic microscopes are scanning type, in which the response to a focused acoustic signal is successively acquired as the beam is mechanically scanned [1-2].

The authors previously proposed a pulse driven ultrasonic sound speed microscopy that can obtain sound speed image in a short time [3-4]. Although a small roughness of the specimen was approved in this type of microscope, slicing the specimen into several micrometers was still required for the observation. However it is often required that the observation can be performed without slicing process, as slicing may damage some functions of the tissue.

Based on the above background, the authors have newly proposed the acoustic impedance microscopy that can image the local distribution of cross sectional acoustic impedance of tissue. As acoustic impedance is given as a product of sound speed and density, it would have a good correlation with sound speed, when the variance in density was not significant. In this paper, the methodology of micro-scale imaging of cross sectional acoustic impedance and its accuracy will be described. As one of the applications, the paper will deal with the observation of cerebellar tissue of a rat.

II. SAMPLE PREPARATION

The cerebellum tissue of a rat was employed as the specimen to be observed. Rats were dissected, and their whole brains were removed. The isolated cerebellums were thickly sliced for both acoustic and optical observations. The 200 μm-thick slices were incubated in oxygenated phosphate buffer solution (PBS) on ice for one hour. They were chemically fixed with 4% formaldehyde fixative, for 20 minutes. For optical observation, some slices were subjected to immunohistochemical staining against calbindin D-28k. The slices were rinsed and observed in same PBS.

The substrate was a flat plastic plate made of polymethylmetacrylate (PMMA), its thickness being 0.5 mm. A reference material, of which acoustic impedance was known, was placed on the same substrate. In many cases, the target tissue was observed together with the reference, in the same field of view.

In this report, a silicone rubber, distilled water or agar was employed as a reference material, choosing one of them depending on the convenience of the measurement. In case of

0-7803-9383-X/05/$20.00 (c) 2005 IEEE

using silicone rubber, the observation was performed after having waited for more than 24 hours since the rubber had been hardened, in order to retain the stability of the material.

III. EXPERIMENTAL SETUP

Fig. 1 illustrates the outline of the acoustic impedance microscope. Distilled water was used for the coupling medium between the substrate and transducer. A sharp electric pulse of about 40 V in peak voltage and 2 ns in width was generated by the pulse generator (AVTEC, AVP-AV-HV3-C). The maximum repetition rate of the pulse was as high as 10 kHz. The transducer was PVDF-TrFE type. It was 1.5 mm in aperture diameter, and 3.0 mm in focal length. An acoustic wave with a wide frequency component was generated by applying the voltage pulse. The acoustic wave, being focused on the interface between the substrate and tissue, was transmitted and received by the same transducer.

The reflection was detected and digitized by the oscilloscope (Tektronix, TDS-7145B). Considering the focal distance and the sectional area of the transducer, the diameter of the focal spot was estimated to be about 50 μm at 80 MHz. The distance between the nearest two points was typically set at 10 μm. Two-dimensional profile of acoustic impedance was obtained by mechanically scanning the transducer using the stage driver, keeping the focal point on the rear surface of the substrate. A typical field of view of 2 mm x 2 mm was covered with 200 x 200 pixels. It took typically 2 - 3 minutes for one observation. In order to save the time for data transfer from the oscilloscope to computer, the waveforms through each X-scan were once stored in the oscilloscope using its fast-frame mode before being transferred through the LAN interface. In order to reduce random noise, three times of responses at the same point were averaged. All the measurements were performed at room temperature.

IV. RESULTS

A. Waveforms

Figure 2 shows the acoustic signal from the reference material. A water droplet was used as the reference. The signal from the target tissue was very similar in waveform but slightly smaller than that from the reference, suggesting the acoustic impedance of the tissue was slightly higher than that of water (1.5×10^6 Ns/m^3). Frequency domain analysis showed that the spectrum was widely spread between 30 - 100 MHz within -12 dB.

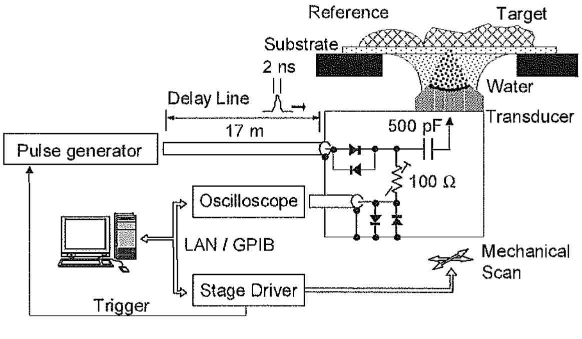

Fig. 1. Schematic diagram of the system.

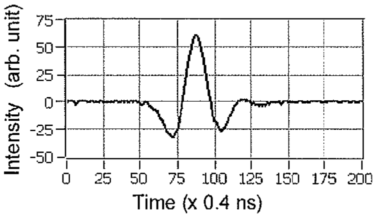

Fig. 2 A reflected acoustic signal.

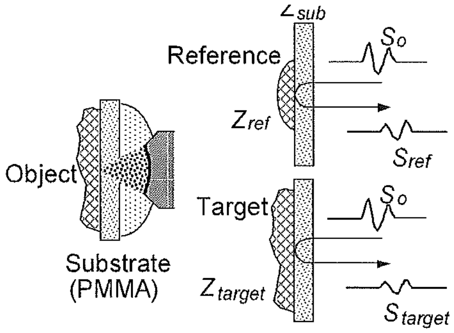

Fig. 3. Illustration for calibration of the acoustic impedance.

B. Calibration

Figure 3 illustrates the calibration of acoustic impedance. The target signal is compared with the reference signal. Hereafter, the signal component at an arbitrary frequency will be symbolized by S. Considering the reflection coefficient, the target signal S_{target} can be described as

$$S_{target} = \frac{Z_{target} - Z_{sub}}{Z_{target} + Z_{sub}} S_0 \qquad (1),$$

where S_0 is the transmitted signal, Z_{target} and Z_{sub} are the acoustic impedances of the target and substrate, respectively. On the other hand, the reference signal can be described as

$$S_{ref} = \frac{Z_{ref} - Z_{sub}}{Z_{ref} + Z_{sub}} S_0 \qquad (2),$$

where Z_{ref} is the acoustic impedance of the reference material. We can measure S_{target} and Z_{ref}, however, cannot directly measure S_0. The acoustic impedance of the target is subsequently calculated as a solution of the simultaneous equations for Z_{target} and S_0, as

$$Z_{target} = \frac{1 - \dfrac{S_{target}}{S_0}}{1 + \dfrac{S_{target}}{S_0}} Z_{sub} = \frac{1 - \dfrac{S_{target}}{S_{ref}} \cdot \dfrac{Z_{sub} - Z_{ref}}{Z_{sub} + Z_{ref}}}{1 + \dfrac{S_{target}}{S_{ref}} \cdot \dfrac{Z_{sub} - Z_{ref}}{Z_{sub} + Z_{ref}}} Z_{sub} \qquad (3),$$

assuming that S_0 is constant throughout the observation process.

In case of using water as the reference, its acoustic impedance was assumed to be 1.5 x 10^6 Ns/m^3. On the other hand, in case of using silicon rubber, the acoustic impedance of itself was calibrated, by using water as the standard reference material. In this report, 0.985 x 10^6 Ns/m^3 was used. The acoustic impedance of agar was calibrated in the same manner short time before the observation. It was calculated to be 1.65 x 10^6 Ns/m^3.

As the sound speed of the substrate at 80 MHz at 25 °C and its density at 25 °C were 2.78 km/s and 1.16 mg/mm^3, respectively, its acoustic impedance was calculated to be 3.22 x 10^6 Ns/m^3.

C. *Evaluation of accuracy*

In order to evaluate the accuracy of acoustic impedance, droplets of saline with different NaCl contents were prepared. Their acoustic impedance was measured using a droplet of distilled water as the reference.

The intensity of the reflected signal was lower with higher acoustic impedance, as the acoustic impedance of the droplets was lower than that of the substrate. The lower signal intensity was subsequently converted into higher acoustic impedance.

Figure 4 shows the result. Each plot represents the average of 600 points, the length of error bar indicating twice the standard deviation. It is seen that the acoustic impedance gradually increases with increasing NaCl content. The dotted curve represents the acoustic impedance as the product of sound speed and density. It agrees well with the measured result. Considering that the acoustic impedance of most of soft biological tissues is distributed between 1.5 - 1.8 x 10^6 Ns/m^3, the result suggests that the accuracy satisfies the requirement for tissue characterization.

D. *Observation of cerebellar cortex of a rat*

Figure 5 illustrates the development of cerebellar cortex [5-6]. Parallel fibers in molecular layer are axons of granule cells and play an important role in cerebella neuronal connections. Migrating granule cells elongate them horizontally and form many excitatory synapses to dendrites of Purkinje cells. These are major neuronal circuits of cerebellum so that parallel fibers are expected to construct rich molecular layer with development. However, it was hard to evaluate a degree of parallel fiber development with over molecular layer. We have little sufficient histochemical tools to visualize the developing parallel fibers.

Figure 6 shows the observed images of cerebellar cortex of a rat at immature (P1; postnatal 1 day), transient (P7), and mature (P20) stages. All the specimens in Fig. 6 had been chemi-

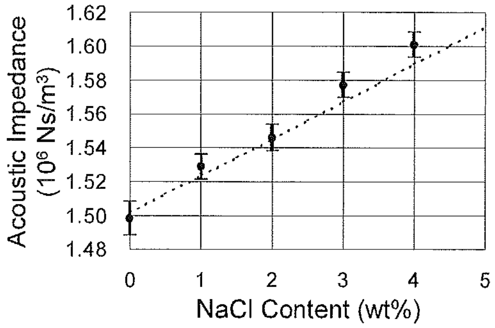

Fig. 4 Acoustic impedance of salt water as a function of NaCl content. Dotted curve indicates the product of sound speed and density.

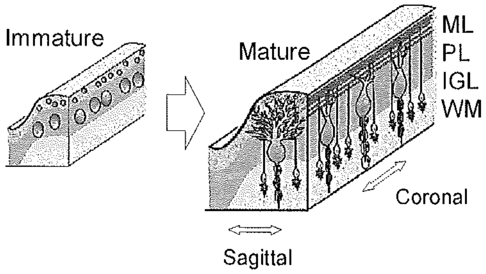

Fig. 5 Illustration for the development of cerabellar cortex.

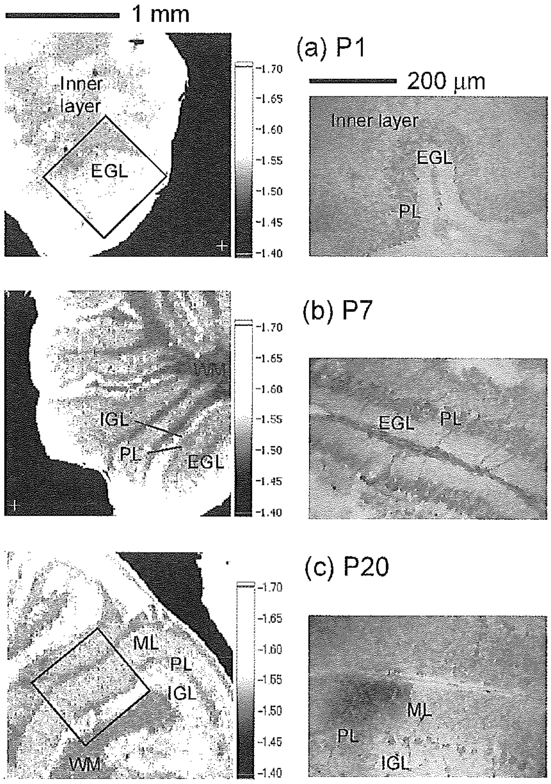

Fig. 6 Two-dimensional profiles of acoustic impedance (x 10^6Ns/m^3) of cerebellar cortex (left) and optical microscopy (right). Specimen: rat, sagittal cross section, chemically fixed. Frequency range: 60-100 MHz.

cally fixed.

In the immature cerebellar cortex (P1), the external granular layer (EGL), the outer layer of the cortex, showed higher impedance compared to the inner layer. The area indicated by the rectangle in the acoustic image is morphologically corresponding to the immunohistochemical observation, although the scale is not completely corresponded because the tissue was somehow subjected to compression during the acoustic observation. At this stage, as myelin is not yet generated, the existence of white matter (WM) is not clearly observed.

In the transient stage, four different layers, the WM, internal granular layer (IGL), Purkinje layer (PL) and EGL become to be comprehensive. The EGL and IGL showed higher impedance than the PL and WM. Morphological correspondence between acoustic and immunohistochemical observation is however not clear in these images.

In the mature stage, the EGL, which is composed of small neuronal cell bodies, has developed into the molecular layer (ML), which is composed of elongated axon (neurite), called parallel fibers. The four layers, WM, IGL, PL and ML are more clearly observed in acoustic image. The correspondence with immunohistological observation is also clearly seen.

It should be noted that very similar images were observed by simply contacting a cross section of the whole tissue with the substrate, without performing chemical fixation.

V. DISCUSSION

Considering the precision of the calibration, the reference material should be stable in both physical and chemical properties, and should strongly adhere to the substrate. It is recommended that the acoustic impedance of the reference be close to that of the target. Furthermore, as for the substrate, most of available materials have higher acoustic impedance than biological tissues. In such cases, the phase of the transmitted signal is reversed at the interface. The acoustic impedance of the substrate should be sufficiently high compared to that of the target, in order to retain a strong reflection. However extremely high acoustic impedance of the substrate may increase the reflection coefficient at the interface between the coupling medium and substrate, and reduce the intensity of transmitted signal to the target. This would obviously reduce the S/N ratio. Therefore, in order to obtain a good S/N ratio, the materials should be carefully selected considering their accordance.

As the transducer was designed for usage with water as the coupling medium, the existence of the plastic plate between the transducer and focal point may bring an aberration. This will be significant if the thickness of the substrate is very thick, and the convergence angle is very large. In this experiment, however, the angle was as small as 4.4 degrees, suggesting the error brought by the aberration would be small. Nevertheless, a quantitative analysis is needed in order to precisely assess the acoustic impedance, especially when a thick substrate is employed.

As the WM is rich with fat, its acoustic impedance would be lower than the IGL. The ML is composed of axon, which has many actin fibers with high elasticity [7]. It would lead to high acoustic impedance. The reason why the Purkinje layer has low impedance is, however, not clear. Further pharmacological investigation is required.

VI. SUMMARY

A new method for two-dimensional acoustic impedance imaging for biological tissue characterization with micro-scale resolution was proposed. Calibration was performed using a reference material of which acoustic impedance was known. Quantitative imaging of acoustic impedance was made possible. Acoustic impedance microscopy with 200 x 200 pixels, its typical field of view being 2 x 2 mm, was obtained by scanning the transducer. Its accuracy, evaluated using saline with various NaCl content, was of satisfactory for characterization of soft tissues. The development of cerebella cultures of a rat was clearly observed as the contrast in acoustic impedance, without staining the specimen. The technique is believed to be a powerful tool for biological tissue characterization, as neither staining nor slicing is required.

ACKNOWLEDGEMENTS

The authors would like to express their sincere thanks to C-K. Lee, T. Morishima and E. Fukushi of Toyohashi University of Technology for their assistance with the experiment. This study was financially supported by Grants-in-Aid for Scientific Research (Scientific Research (B)15360217, (B) 15300178), and Japan Society for the Promotion of Science and Health and Labor Sciences Research Grants from the Ministry of Health, Labor and Welfare for the Research on Advanced Medical Technology (H17-Nano-001).

REFERENCES

[1] Y. Saijo, M. Tanaka, H. Okawai, H. Sasaki, S. Nitta & F. Dunn: "Ultrasonic Tissue Characterization of Infarcted Myocadium by Scanning Acoustic Microscopy", *Ultrasound in Med. & Biol.*, 23-1, 77 (1997).

[2] H. Okawai, K Kobayashi & S. Nitta: "An Approach to Acoustic Properties of Biological Tissues Using Acoustic Micrographs of Attenuation Constant and Sound Speed", *J. Ultrasound Med.*, 20, 891 (2001).

[3] N. Hozumi, R. Yamashita, C-K Lee, M. Nagao, K. Kobayashi, Y. Saijo, M. Tanaka, N. Tanaka & S Ohtsuki: "Ultrasonic Sound Speed Microscope for Biological Tissue Characterization Driven by Nanosecond Pulse", *Acoustic Science & Technology*, 24, 386 (2003).

[4] N. Hozumi, R. Yamashita, C-K. Lee, M. Nagao, K. Kobayashi, Y. Saijo, M. Tanaka, N. Tanaka & S.Ohtsuki: "Time –frequency analysis for pulse driven ultrasonic microscopy for biological tissue characterization", *Ultrasonics*, 42, 717 (2003).

[5] D. H. Sanes, T. A. Reh & W. A. Harris: *Development of the Nervous System*, Academic Press (2000).

[6] E. R. Kandel, J. H. Schwarts & T. M. Jessell: *Principles of Neural Science*, McGraw-Hill (2000).

[7] HW. Wu, T. Kuhn & VT. Moy: "Mechanical Properties of L929 Cells Measured by Acoustic Force Microscopy: Effects of Anticytoskeltal Drugs and Membrane Crosslinking", *Scanning*, 20, 389 (1998).

Speed of Sound Microscopy for Biomedical Applications

Y. Saijo, H. Sasaki, T. Yambe, M. Tanaka
Department of Medical Engineering and Cardiology
Institute of Development, Aging and Cancer, Tohoku University
4-1 Seiryomachi, Aoba-ku, Sendai 980-8575, Japan
saijo@idac.tohoku.ac.jp

N. Hozumi
Department of Electrical and Electronic Engineering
Graduate School, Toyohashi University of Technology
1-1 Tempaku, Toyohashi, 441-8580, Japan

K. Kobayashi, N. Okada
Research & Development Headquarters
Honda Electronics Co. Ltd.
20 Oyamazuka, Oiwa-cho, Toyohashi, 441-3193, Japan

Abstract — **We have been developing a scanning acoustic microscope (SAM) system for medicine and biology featuring quantitative measurement of ultrasonic speed and attenuation of soft tissues. In the present study, we will propose a new concept ultrasonic speed microscopy that can measure the thickness and ultrasonic speed using fast Fourier transform of a single pulsed wave instead of continuous waves used in conventional SAM systems. Six coronary arteries were frozen and sectioned approximately 10 μm in thickness. They were mounted on glass slides without cover slips. The scanning time of a frame with 300×300 pixels was 90 s and two-dimensional distribution of speed of sound was obtained. The speed of sound was 1720 m/s in the thickened intima with collagen fiber, 1520 m/s in lipid deposition underlying fibrous cap and 1830m/s in calcified lesion in the intima. These basic measurements will help understanding echo intensity and pattern in intravascular ultrasound (IVUS) images.**

Keywords; acoustic microscopy, ultrasonic speed, coronary artery, atherosclerosis

I. INTRODUCTION

We have been developing a scanning acoustic microscope (SAM) system for biomedical use since 1985. We have been investigating the acoustic properties of various organs and disease states by using this SAM system. In the areas of medicine and biology, scanning acoustic microscopy (SAM) has three main objectives. The first, SAM is useful for intraoperative pathological examination because it doesn't require a special staining. The second, SAM provides basic data for understanding lower frequency medical ultrasound images such as echocardiography or intravascular ultrasound. The third, SAM can be used to assess biomechanics of tissues and cells at a microscopic level. The originality of the previous SAM system of Tohoku University lies in providing quantitative values of attenuation and speed of sound in thin slices of soft tissue. Although the system may be currently in use, it was constructed using precise hand-crafted technologies and analog signal acquisition circuits. Besides, the previous system needed repeated acquisitions for calculation of quantitative values because it used continuous waves of different frequencies.

Recently, we have proposed a prototype of speed of sound microscopy using a single pulsed wave instead of continuous waves used in conventional SAM systems. In the present study, we construct a compact, commercially available speed of sound microscopy and evaluate the system performance by measuring normal and atherosclerotic coronary arteries.

II. METHODS

A. *Tissue Preparation*

Normal and atherosclerotic human coronary arteries were obtained from autopsy. The specimens were rinsed in PBS (phosphate buffer saline) and immersed in 10% to 30% sucrose solutions. Then the specimens were embedded in OCT (optimal cutting temperature) compound and rapidly frozen by liquid nitrogen at −20°C. The specimens were sliced approximately 10 microns by a cryostat and mounted on a silane-coated glass slides.

B. Speed of Sound Microscopy

Fig. 1 shows a block diagram of speed of sound microscopy for biological tissue characterization. A single ultrasound pulse with a pulse width of 6 ns was emitted and received by the same transducer above the specimen. The aperture diameter of the transducer was 1.2 mm, and the focal length was 1.5 mm. The central frequency was 80 MHz, the bandwidth was 40-150 MHz, and the pulse repetition rate was 10 kHz. The diameter of the focal spot was estimated to be 20 μm at 80 MHz by taking into account the focal distance and sectional area of the transducer. Distilled water was used as the coupling medium between the transducer and the specimen. The reflections from the tissue surface and those from the interface between the tissue and glass were received by the transducer and were introduced into a Windows-based PC (Pentium 4, 2.8 GHz, 1GB RAM, 80GB HDD) via an analogue-digital converter (Acqiris DP-210, Geneva, Switzerland). The frequency range was 500 MHz, and the sampling rate was 2 GS/s. Eight values of the time taken for a pulse response at the same point were averaged in order to reduce random noise.

The transducer was mounted on an X-Y stage with a microcomputer board that was driven by the PC through RS232C. The Both X-scan and Y-scan were driven by linear servo motors. Finally, two-dimensional distributions of ultrasonic intensity, speed of sound, attenuation coefficient and thickness of a specimen measuring 2.4×2.4 mm were visualized using 300×300 pixels. The total scanning time was 90 s.

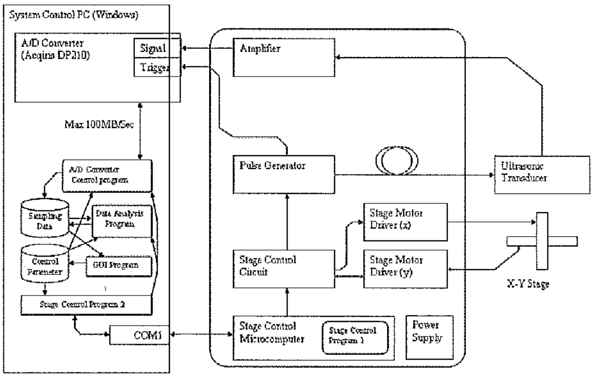

Figure 1. Block diagram of speed of sound microscopy.

Fig. 2 shows the appearance of the speed of sound microscopy. Whole system are on the desktop.

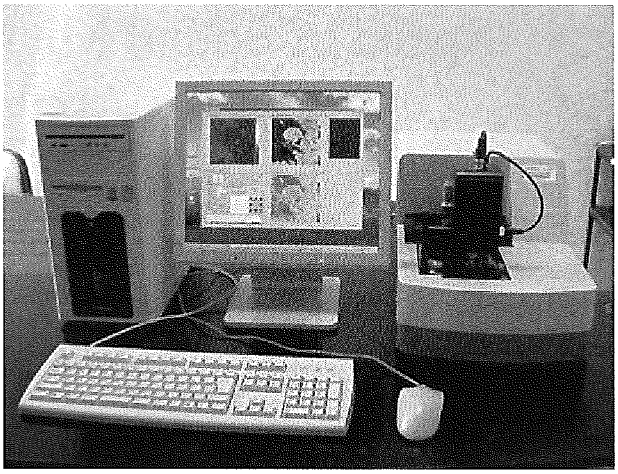

Figure 2. Apperance of the speed of sound microscopy.

C. Signal Analysis [10]

The reflected waveforms are shown in Fig. 3. The waveform at the glass surface without the tissue is shown in (a). This signal was used as a reference waveform. The decline of the glass surface was compensated by measuring three different points in the glass area surrounding the tissue. The waveform from the tissue area is shown in (b). Although the waveform contains two reflections at the surface and at the interface of the tissue and glass, the two components cannot be separated in time domain analysis. Thus, frequency domain analysis was performed by analyzing the interference between the two reflections. Intensity and phase spectra were calculated by Fourier transforming the waveform. The spectra were normalized by the reference waveform. Fig. 4 shows the frequency domain analysis of the interfered waveform.

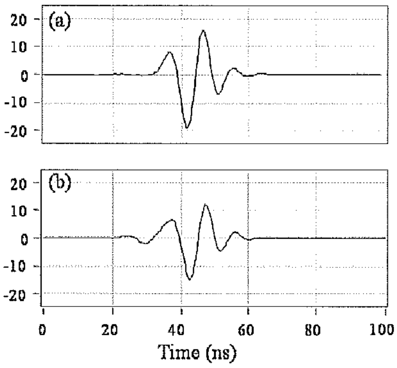

Figure 3. Reflected waveforms (a) from the glass surface without tissue, and (b) from the tissue area

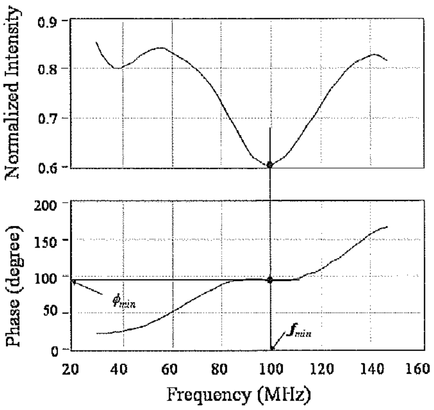

Figure 4. Frequency domain analysis of interfered waveform. f_{min}: the minimum point in the intensity spectrum, ϕ_{min}: corresponding phase angle

Denoting the minimum point in the intensity spectrum by f_{min} and the corresponding phase angle by ϕ_{min}, the phase difference between the two reflections at the minimum point is $(2n-1)\pi$, which yields

$$2\pi f_{min} \times \frac{2d}{c_o} = \phi_{min} + (2n-1)\pi \qquad (1)$$

where d, c_o, and n are the tissue thickness, speed of sound in water, and a non-negative integer, respectively.

The phase angles ϕ_{min} can be expressed by

$$2\pi f_{min} \times 2d\left(\frac{1}{c_o} - \frac{1}{c}\right) = \phi_{min} \qquad (2)$$

since ϕ_{min} is the phase difference between the wave that travels the distance $2d$ with speed of sound c and the wave that travels a corresponding distance with speed of sound c_o. By solving equations (1) and (2),

$$d = \frac{c_o}{4\pi f_{min}}\{\phi_{min} + (2n-1)\pi\} \qquad (3)$$

is obtained for the minimum point.

Finally, the speed of sound at each frequency is calculated as

$$c = \left(\frac{1}{c_o} - \frac{\phi_{min}}{4\pi f_{min} d}\right) \qquad (4)$$

After determination of the thickness, attenuation of ultrasound was then calculated by dividing amplitude by the thickness and frequency.

III. RESULTS

Fig. 5 shows a PC window of our ultrasonic speed microscopy. The upper left is an amplitude image, the upper right is an ultrasonic speed image, the lower left is an attenuation image and the lower right is the thickness distribution of the normal coronary artery. The intima is thin and speed of sound is 1600 m/s in the intima, 1560 m/s in the media and 1590 m/s in the adventitia, respectively.

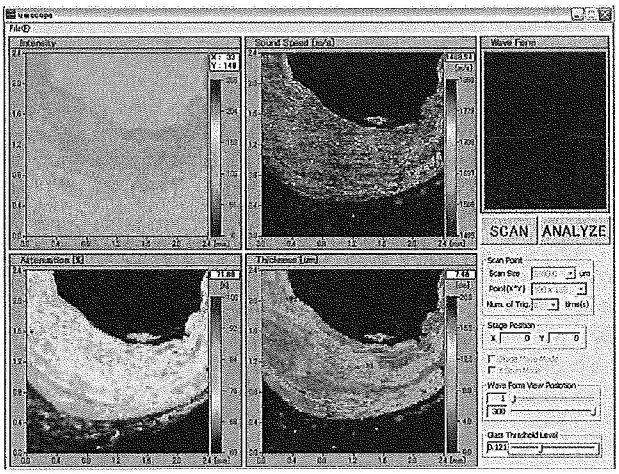

Figure 5. PC window of speed of sound microscopy showing a normal coronary artery. Upper left: amplitude image, upper right: speed of sound image, lower left: attenuation image and lower right: thickness

Fig. 6 is an atherosclerotic coronary artery. The speed of sound is 1680 m/s in the thickened intima with collagen fiber, 1520 m/s in lipid deposition underlying fibrous cap and 1810m/s in calcified lesion in the intima.

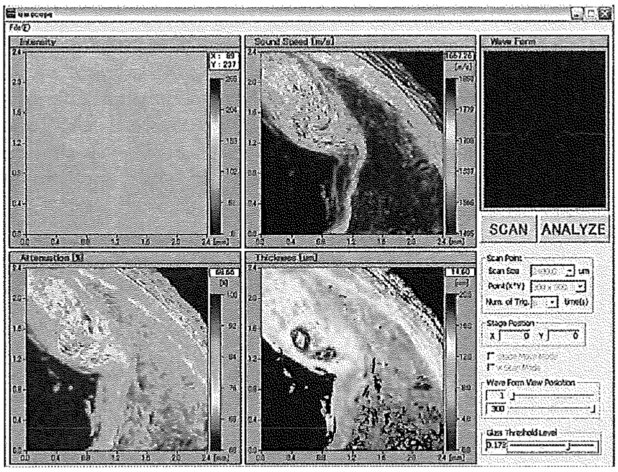

Figure 6. PC window of speed of sound microscopy showing an atherosclerotic coronary artery. Upper left: amplitude image, upper right: speed of sound image, lower left: attenuation image and lower right: thickness.

IV. DISCUSSION

In the present study, speed of sound in the excised human coronary arteries was measured with the ultrasonic speed microscopy. The results would become basic data base for interpretation of clinical IVUS images and novel IVUS imaging technologies.

The results showed that the speed of sound in the intima and adventitia, mainly consisted of collagen fiber, had higher values than those of media, mainly consisted of vascular smooth muscle. The different of acoustic properties may lead to the classical three-layered appearance of normal coronary artery in clinical IVUS imaging. The findings indicate that the echo intensity is not determined by the difference of acoustic impedance between neighboring layers. The distribution and the structure of materials with different acoustic properties may also contribute to the echo pattern in IVUS.

The plaque with a thick fibrous cap consisted of collagen fiber, considered showed higher value of speed of sound than those of normal media. Generally, absorption and scattering are the two main factors of attenuation of ultrasound. Thus, the high scattering within the thickened intima may lead to the high intensity echo in the "hard plaque". Lipid showed speed of sound. These values explain the low echo in the "soft plaque" in the same manner of renal cysts containing water like fluid. Besides its absolute low values, the homogeneity of acoustic properties within the lipid pool may contribute to the low scattering and consequently a lipid pool shows low intensity echo.

V. CONCLUSIONS

An acoustic microscope system that can measure the speed of sound of thin slices of biological material was developed. It was a unique acoustic microscope because it used a single pulse and the Fourier transform to calculate the speed of sound at all measuring points. Although the data acquisition time of a single frame was greater than that in conventional SAM, the total time required for calculation was significantly shorter. The acoustic microscope system can be applied to intraoperative pathological examination..

ACKNOWLEDGMENTS

This study was supported by Grants-in-Aid for Scientific Research (Scientific Research (B) 15300178, Scientific Research (B) 15360217) from the Japan Society for the Promotion of Science and Health and Labor Sciences Research Grants from the Ministry of Health, Labor and Welfare for the Research on Advanced Medical Technology (H17-Nano-001).

REFERENCES

[1] Y. Saijo, M. Tanaka, H. Okawai, F. Dunn, The ultrasonic properties of gastric cancer tissues obtained with a scanning acoustic microscope system, Ultrasound Med Biol 17 (1991), pp. 709-714.

[2] H. Sasaki, M. Tanaka, Y. Saijo, H. Okawai, Y. Terasawa, S. Nitta, K. Suzuki, Ultrasonic tissue characterization of renal cell carcinoma tissue, Nephron 74 (1996) , pp. 125-130.

[3] Y. Saijo, M. Tanaka, H. Okawai, H. Sasaki, S. Nitta, F. Dunn, Ultrasonic tissue characterization of infarcted myocardium by scanning acoustic microscopy, Ultrasound Med Biol 23 (1997), pp. 77-85.

[4] Y. Saijo, H. Sasaki, H. Okawai, S. Nitta, M. Tanaka, Acoustic properties of atherosclerosis of human aorta obtained with high-frequency ultrasound, Ultrasound Med Biol 24 (1998) , pp. 1061-1064.

[5] Y. Saijo, H. Sasaki, M. Sato, S. Nitta, M. Tanaka, Visualization of human umbilical vein endothelial cells by acoustic microscopy, Ultrasonics 38 (2000) , pp. 396-399.

[6] Y. Saijo, T. Ohashi, H. Sasaki, M. Sato, C.S. Jorgensen, S. Nitta, Application of scanning acoustic microscopy for assessing stress distribution in atherosclerotic plaque, Ann Biomed Eng 29 (2001) , pp. 1048-53.

[7] H. Sasaki, Y. Saijo, M. Tanaka, S. Nitta, Influence of tissue preparation on the acoustic properties of tissue sections at high frequencies, Ultrasound Med Biol 29 (2003) , pp. 1367-72.

[8] Y. Saijo, T. Miyakawa, H. Sasaki, M. Tanaka, S. Nitta, Acoustic properties of aortic aneurysm obtained with scanning acoustic microscopy, Ultrasonics 42 (2004) , pp. 695-698.

[9] H. Sano, Y. Saijo, S. Kokubun, Material properties of the supraspinatus tendon at its insertion – A measurement with the scanning acoustic microscopy, J. Musculoskeletal Res. 8 (2004) , pp. 29-34.

[10] N. Hozumi, R. Yamashita, C.K. Lee, M. Nagao, K. Kobayashi, Y. Saijo, M. Tanaka, N. Tanaka, S. Ohtsuki, Time–frequency analysis for pulse driven ultrasonic microscopy for biological tissue characterization, Ultrasonics 42 (2004) , pp. 717-722.

Coronary Plaque Classification through Intravascular Ultrasound Radiofrequency Data Analysis Using Self-organizing Map

***Takahiro Iwamoto*[1], *Akira Tanaka*[2], *Yoshifumi Saijo*[3], *and Makoto Yoshizawa*[4]**
[1] Graduate School of Engineering, Tohoku University, Sendai, JAPAN
[2] Faculty of Symbiotic Systems Science, Fukushima University, Fukushima, JAPAN
[3] Institute of Development, Aging and Cancer, Tohoku University, Sendai, JAPAN
[4] Information Synergy Center, Tohoku University, Sendai, JAPAN

Abstract— **Intravascular ultrasound (IVUS) is an important clinical tool in the assessment of atherosclerotic plaque in coronary artery diseases. Using IVUS, we can obtain high resolution echo image of cross-sections of the coronary artery. However, it is difficult to accurately classify plaques by using the echogram only. We propose a method of IVUS Radiofrequency (RF) signal classification using self-organizing map (SOM). Characteristic ROIs (region of interest) of the IVUS echogram of patients with coronary lesions were selected by an expert medical doctor, and the SOM learned from these ROIs. The SOM could classify the RF signals with accuracies of 95.9% for fibrous plaque, 99.5% for blood, 96.2% for calcified plaque and 16.3% for media regions. This result suggests that the proposed technique is useful for automatic characterization of plaque in coronary artery.**

Keywords-; Intravascular ultrasound, Self organizing map, tissue characterization, Spectrum analysis

I. INTRODUCTION

Rupture of vulnerable atherosclerotic plaque is the cause of most acute coronary syndromes.

Accurate *in vivo* identification of plaque components may allow the detection of vulnerable atheroma before rupture. IVUS allows the visualization of cross-sections of coronary artery with atherosclerotic plaques *in vivo* [1]-[5]. In standard IVUS gray-scale images, calcified plaque regions and dense fibrous components generally reflect ultrasound energy well and thus appear bright and homogeneous in IVUS images. They are usually labeled as "hard" plaque. Conversely, regions of low echo reflectance in IVUS images are usually labeled as "soft" plaque [6]. However, the visual interpretation is limited in the assessment of quantitative plaque composition. But, spectral analysis of the radiofrequency (RF) ultrasound signals may allows detailed assessment of plaque composition.

Therefore, the goal of this study was to compare real-time determination of plaque components, using easily accessible IVUS backscattered signals. With the use of a combination of spectral parameters, classification schemes were developed for the analysis of IVUS data, and the RF spectral information was used to reconstruct tissue maps.

II. METHOD

RF Signal data were acquired from 14 human left anterior descending (LAD) coronary arteries at PTCA (percutaneous transluminal coronary angioplasty). The average age was 72 ± 12 years.

A. Data Acquisition

IVUS data were acquired with an IVUS console "Clear View Ultra" (Boston Scientific Inc, USA) and 40MHz, mechanically rotating IVUS catheter "Atlantis SR Plus" (Boston Scientific Inc, USA).

RF data were digitized and stored in a PC (Dell Precision Workstation 330, Dell Inc, USA) using an A/D board "GAGE compuscope 8500" (500Msamples/sec., with 8 bits of resolution, Gage Applied Inc, Montreal, Canada) for off-line analysis.

B. IVUS Data Analysis

IVUS RF signal from the ROIs selected by the expert medical doctor were processed in MATLAB 6.5 (The MathWorks Inc, USA) as follows.

Initially, a band-pass filter (15MHz-105MHz) was applied to the IVUS RF signal data. Then each line in the ROI is scanned by a 128-points width hamming window. The frequency spectrum is calculated for each position of the hamming window using a mathematical autoregressive (AR) model

AR processes are known to be more appropriate for short data records, such as IVUS signals, than discrete Fourier

---

Acknowledgements: This study was supported by Grants-in-aid from Japan Society of Promotion of Science (15300178) and Grants-in-aid from Ministry of Health, Labour and Welfare (H17-nano-001).

transforms and have been shown to result in high resolution spectral estimates [7].

Preliminary tests in this study estimated the optimum AR model order (order 15 via Akaike's final prediction error method [8]) for characterizing plaque components, after tests with several models.

Further, the optimized AR spectra were used to compute 18 spectral shape parameters for each ROI. These parameters were: fundamental wave power, frequency of fundamental wave power, second harmonic wave power, frequency of harmonic wave power, local minimum power between fundamental wave power and second harmonic wave power, frequency of local minimum power, maximum power, frequency of maximum power, slope from power at frequency 15MHz to fundamental wave power, corresponding y-intercept, slope from fundamental wave power to local minimum power, corresponding y-intercept, slope from local minimum power to second harmonics power, corresponding y-intercept, slope from second harmonics power to 100MHz power, corresponding y-intercept, mean of integrated backscatter, ROI position at line.

C. Training data and test data

ROIs for training data and test data were selected from IVUS B-mode images by an expert medical doctor. These IVUS B-mode images were reconstructed from the RF data by software written by our group. Then three plaque types (fibrous, calcified and other plaque) and four structure types (catheter, shade of guide-wire, blood, and media) were defined. 75% of these data were used as training data of the SOM classifier. The rest of these data was used as test data of the SOM classifier.

D. SOM

After the training, the SOM classifier was used to classify IVUS RF signals.

The SOM is a neural network based on unsupervised learning proposed by T. Kohonen [9]. It is a vector quantization method which places the prototype vectors on a regular low-dimensional grid in an ordered fashion. This makes the SOM a powerful visualization tool. A SOM consists of neurons organized on a regular low-dimensional grid. Each neuron is a d-dimensional weight vector (prototype vector, codebook vector) where d is equal to the dimension of the input vectors.

The neurons are connected to adjacent neurons by a neighborhood relation, which dictates the topology, or structure, of the map.

E. SOM Training Settings

The SOM training settings were as follows.

Map size was 25 × 17 of hexagonal lattice (numbers of neuron was 425). Training phase was 20,000 times. A batch training algorithm was used, the data set were presented to the SOM as a whole, and the new weight vectors were weighted averages of the data vectors [10].

F. Labeling Each neuron at SOM

After training, the neurons of the SOM were labeled in accordance with the representatives vectors of the training data. Each label was decided based on the major component of the group.

Using this labeled SOM, the ROIs were classified.

G. Plaque Classification

The SOM classifier learned the plaque component type by using spectral parameters.

At each line in ROIs, frequency spectra of samples within the window were calculated, and spectral shape parameters were derived. The plaque types were classified based on these parameters.

The window was then moved by one sample, and data were reanalyzed.

Hence, each sample was given a particular value corresponding to one of the 7 components (catheter, shade of guide-wire, blood, calcified plaque, fibrous plaque, media, and other).

The results were validated through classifying data that were used in the SOM training to determine predictive accuracy, sensitivity, and specificity from widely accepted equations in biomedical literature [11].

Color codes were assigned to the plaque component values, and the tissue maps were reconstructed on IVUS B-mode images by our algorithm.

These tissue maps were then checked by an expert medical doctor to assess the plaque characterization.

III. RESULTS

Twenty-three plaque ROIs were identified in a group of 14 vessel images.

ROIs were selected by an expert medical doctor for catheter (n=21), shade of guide-wire (n=18), blood (n=15), fibrous